NANO EXPRESS

Tunable Nanostructures and Crystal Structures in Titanium Oxide Films

**A. K. Srivastava · M. Deepa · S. Bhandari ·
H. Fuess**

Abstract Controllable nanostructures in spin coated titanium oxide (TiO$_2$) films have been achieved by a very simple means, through change of post deposition annealing temperature. Electron beam imaging and reciprocal space analysis revealed as-deposited TiO$_2$ films to be characterized by a dominant anatase phase which converts to the rutile form at 600 °C and reverts to the anatase modification at 1,200 °C. The phase changes are also accompanied by changes in the film microstructure: from regular nanoparticles (as-deposited) to nanowires (600 °C) and finally to dendrite like shapes at 1,200 °C. Photoluminescence studies, Raman spectral results, and X-ray diffraction data also furnish evidence in support of the observed solid state phase transformations in TiO$_2$.

Keywords Nanostructured TiO$_2$ · Phase transformations · Photoluminescence · Spectroscopy

Introduction

Nanostructured materials are of great interest due to their tunable microstructure, phase transformations and quantum confinements, required for potential usage [1–3]. Among these nano—particles, wires, rings, combs, tetrapods of materials such as ZnO [4–8], WO$_3$ [9–12], and TiO$_2$ [13–21] are most desired for various semiconducting, electrochromic, and mechanical applications. TiO$_2$ has been reported a versatile material, required for sensors [22], optical devices [15, 16, 23, 24], photocatalysis [25], photoelectrochemical [26–28], tribological [29, 30], and bio-compatible surgical instruments [31, 32]. Recently thermally evaporated TiO$_2$ nanowires have been examined and an efficient photoluminescence was registered in the blue region [13]. In our preliminary observations [16] a correlation between microstructural features of sol–gel derived TiO$_2$ and photoluminescence has been attempted.

The applications of TiO$_2$ pertaining to engineering, semiconducting, and medicinal industries are enormous and expected to enhance by manifold times if the material is nanostructured to design fundamental nanodevices. However, detailed experimental studies on crystalline phases and the stability of microstructures of TiO$_2$ that normally are temperature dependent are imperative to enable their use for any practical device. In this context, the present report provides a systematic evaluation of phase transformations and morphological features of TiO$_2$ films by use of electron beam imaging and corresponding reciprocal space interpretations. These nano-scaled modifications upon annealing complement Raman and photoluminescence spectroscopic results.

Experimental Details

Titanium oxide powder (Degussa, P25) was used as received. The powder was sonicated in polyethylene glycol 400 and the resulting white, homogeneous dispersion was spin coated at 3,500 rpm for 30 s on SnO$_2$:F coated glass-substrates. Subsequently these films were subjected for annealing at different temperatures, viz., 450, 500, 600, and 700 °C for 2 h. This dispersion was heat treated in an

A. K. Srivastava (✉) · M. Deepa · S. Bhandari
Division of Materials Characterization, National Physical
Laboratory, Dr. K.S. Krishnan Road, New Delhi 110012, India
e-mail: aks@nplindia.ernet.in

H. Fuess
Technische Universität Darmstadt,
Darmstadt D-64287, Germany

alumina crucible at 1,100 and 1,200 °C for the same duration. The powder was then grounded for 1 h and then re-dispersed in ethanol. The resulting suspension was spin coated and the films were heat treated at 150 °C. A transmission electron microscope (TEM, model FEI CM12) was employed for microstructural imaging and phase analysis. Several samples of TiO_2 for TEM characterization were prepared by a careful removal of these films from the substrate using a sharp-edged surgical blade. In this process the films with 1–2 mm in dimension were possible to load on commercially available copper grids (diameter: 3.05 mm) of 200 mesh-pore size. Surface morphology was characterized with an environmental scanning electron microscope (SEM, model Hitachi TM1000). Photoluminescence investigations were performed on a Perkin Elmer LS-55 luminescence spectrometer and Raman spectra were recorded on a Perkin-Elmer GX 2000 OPTICA spectrophotometer.

Results and Discussion

Evolution of Microstructures and Phase Transformations

The bright field micrograph of an as-deposited TiO_2 film (Fig. 1a) shows the film to be constituted by randomly distributed particles, 2–10 nm in size. At higher magnifications, polyhedral morphologies of nanoparticles with well-defined facets were observed (Fig. 1b). A corresponding selected area electron diffraction pattern (SADP) shows the Debye rings in reciprocal space (Fig. 2a) which arise from the anatase crystal structure (body centered tetragonal and space group $I4_1/amd$) of TiO_2 with lattice constants $a = 0.38$ nm and $c = 0.95$ nm. The planes of anatase (101, 004, 200, 105, 211) structure are marked on the different rings in SADP (Fig. 2a).

Annealing the as-deposited TiO_2 film at 450 °C is accompanied by grain growth as uniformly distributed particles of 10–25 nm dimensions were observed (Fig. 3a) in the annealed film. The corresponding SADP comprises additional rings (as compared to the SADP of as-deposited film in Fig. 2a) and these new rings belong to the rutile crystal structure (primitive tetragonal; space group $P4_2/mnm$) of TiO_2 with lattice constants $a = 0.45$ nm and $c = 0.29$ nm. The existence of two-phase mixture in the film annealed at 450 °C is indicative of initiation of solid-state phase transformation and this phase transformation does not get completed even at 600 °C, as even at this temperature both rutile and anatase phases were found to be co-existent in the film (SADPs not shown here). The nanoparticulate morphology does not register much change as annealing temperature was raised from 450 to 500 °C
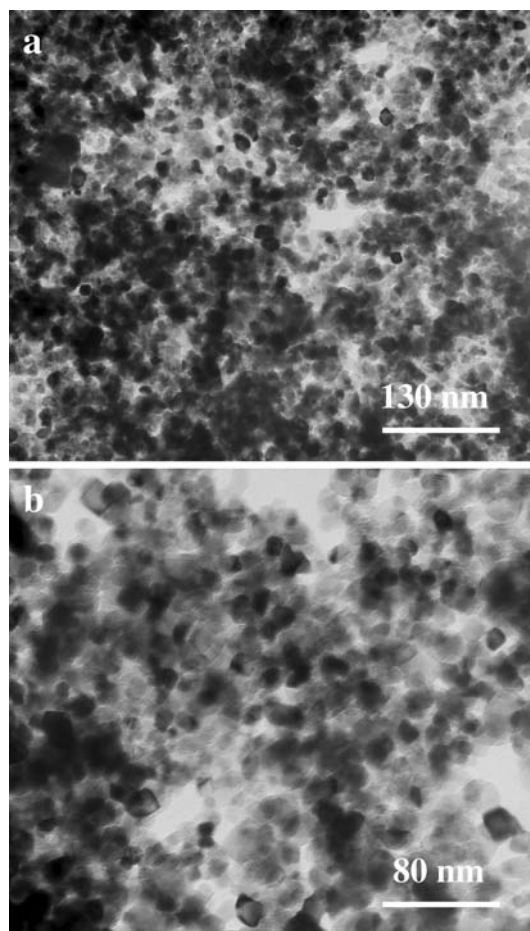

Fig. 1 TEM bright field micrographs of nanoparticles in as-deposited condition showing **a** homogeneous distribution and **b** different shape and size

and this can be easily perceived from Fig. 3b. But particle size grows visibly when the film was annealed at 600 °C (Fig. 3c). On increasing the annealing temperature to 700 °C, a substantial transformation of crystal structure and microstructure of TiO_2 was registered. The film now has a smooth faceted surface and particles size lies in the range of 30–60 nm and the grain shapes are largely cubical and euhedral (Fig. 4a–c). The corresponding SADP shows a complete phase transformation from anatase to rutile crystal structure with lattice constants $a = 0.45$ nm and $c = 0.29$ nm. The corresponding planes (110, 101, 111, 211, 002) are marked on the Debye rings in SADP (Fig. 2c) and no planes related to the anatase phase were seen. At this temperature, elongated wire type structures were also formed. One such nanowire of about 40 nm diameter with a length of about 100 nm is shown in Fig. 4c. Formation of nanowires indicates a preferred growth of certain high-density crystallographic planes of rutile phase at the lattice scale. This variation in particle shapes as a function of annealing temperature is also illustrated schematically in
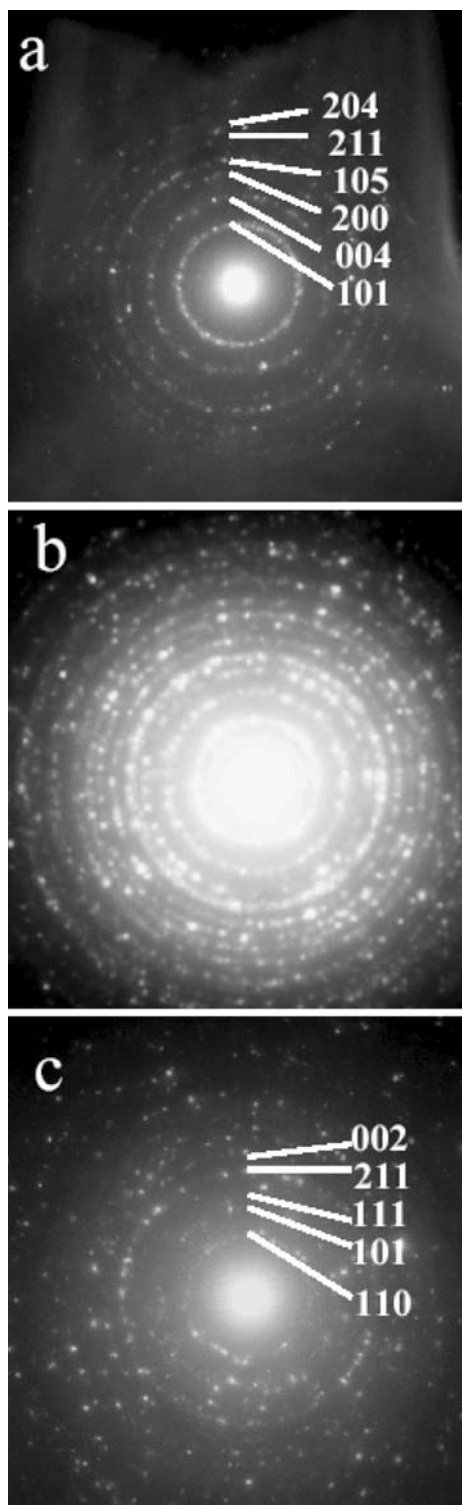
Fig. 2 Selected area electron diffraction patterns recorded from samples of **a** as deposited and different annealing conditions; **b** 450 °C and **c** 700 °C

Fig. 5. Attempts were made to correlate the grain coarsening and annealing temperature to fit with an exponential function, to obtain a general trend of heating on such
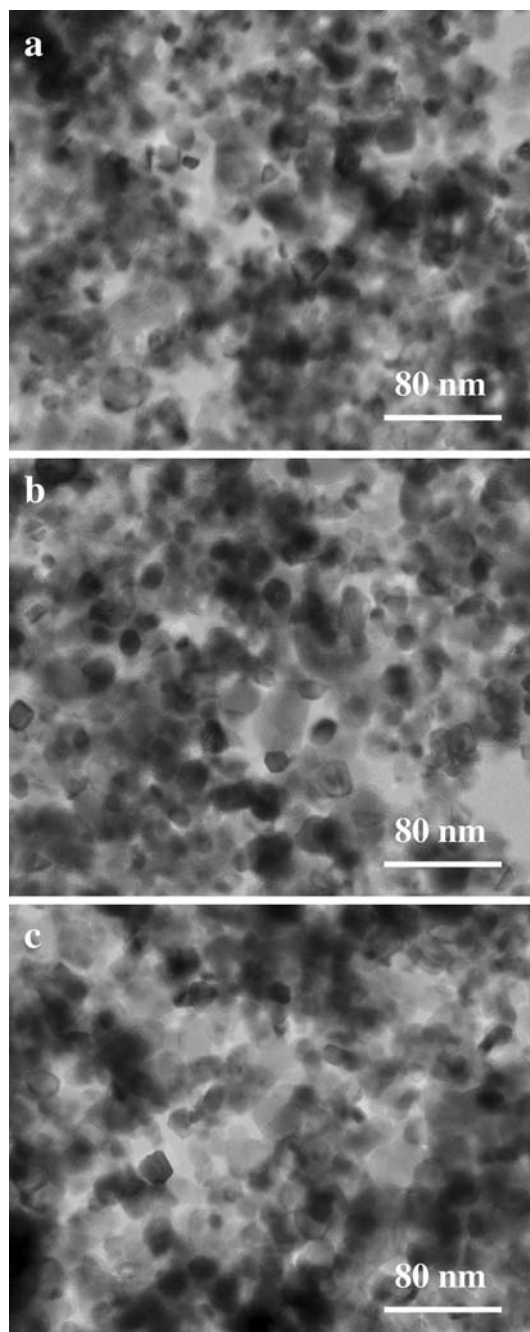

Fig. 3 TEM bright field micrographs of nanoparticles in different annealing conditions; **a** 450 °C, **b** 500 °C and **c** 600 °C

oxides. The continuous curve was drawn after data fitting (Fig. 5) with an equation of the form: $y = c \exp. (x/t)$, where y and x are coordinate axes representing particle size and annealing temperature, respectively. The constants c and t are 5.17 and 2.34, respectively.

The mechanism for the solid state phase transformation from anatase to rutile at high temperatures is not clear, especially when the particle size is of the order of tens of nanometers. We conjecture that on annealing as-deposited
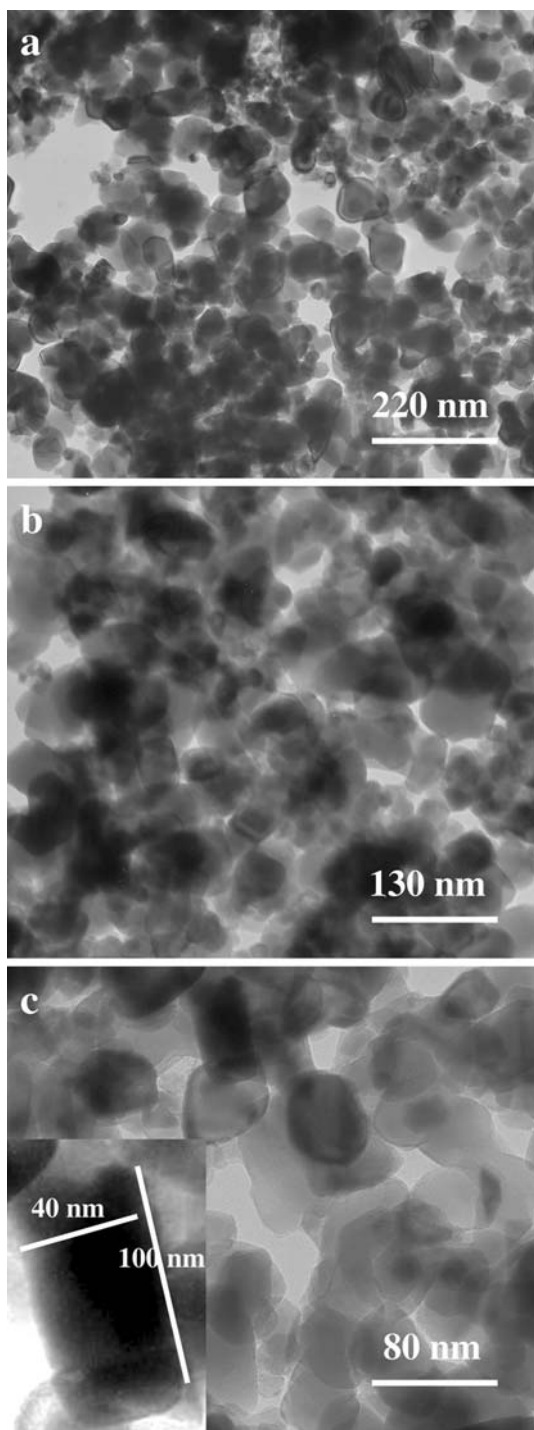
Fig. 4 TEM bright field micrographs (**a**–**c**) of nanoparticles annealed at 700 °C

Fig. 5 Graphical presentation of size of nanoparticles with annealing temperature. A corresponding data fitted polynomial $y = c$ exp. (x/t) showing a good agreement between theory and experiment

more dense ($\rho = 4.25$ g cm^{-3}) compared to anatase ($\rho = 3.894$ g cm^{-3}). Although both anatase and rutile phases are tetragonal, but the rutile structure is close to cubic. The cubic structure is known to be the most symmetrical lattice ($c/a = 1$) and thermodynamically most stable. During the crystallographic transition, the movement of atoms is such that the highest atomically dense plane (101) of the anatase phase becomes the second most intense plane of the rutile structure. Moreover the (110) plane evolves as the highest atomically dense plane in the rutile structure, which is not a preferred plane for atomic sites in the anatase form. Recently the transformation from anatase to rutile on annealing at the temperature about 800 °C has been investigated by Wu et al. [13]. Figure 6 represents a schematic, delineating these two planes: 110

Fig. 6 Schematics of anatase- and rutile- unit cells marked with 101 and 110 planes and lattice points

TiO$_2$, the rearrangement of Ti and O atoms is such that the unit cell of TiO$_2$ tries to be more uniform in all three axes (a,b,c) to attain a more stable and defect-free configuration. This phenomenon reduces the value of c/a from 2.51 (anatase) to 0.65 (rutile) significantly and hence the volumes of basic unit cell as well. The unit cell of rutile is
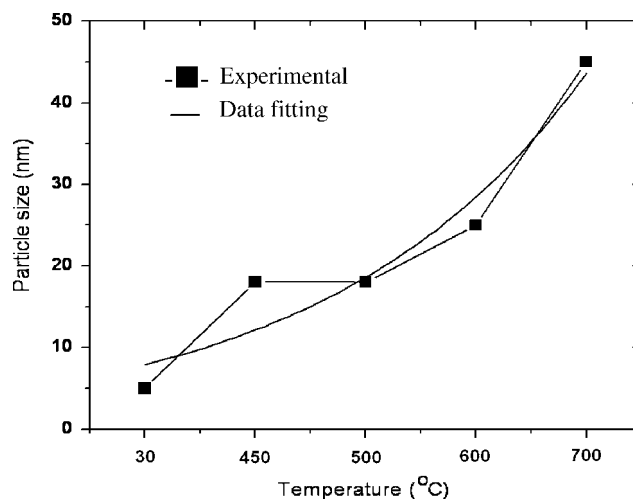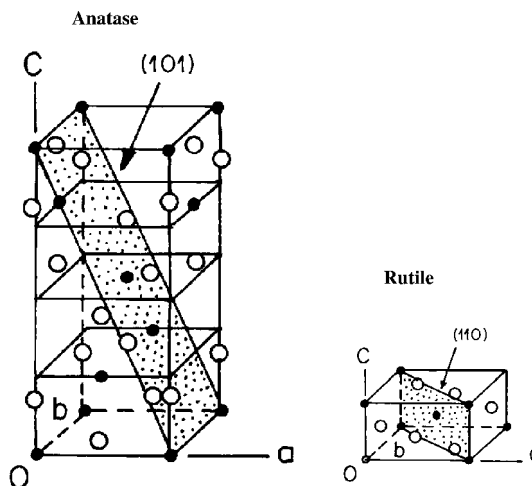
and 101 in anatase and rutile unit cells, respectively, of TiO$_2$. This is remarkable as the 110 plane of rutile has also been found to be responsible for the growth of TiO$_2$ nanowires [13] with a single crystalline structure.

In a similar fashion, here annealing at 700 °C steers the preferred growth under specific crystallographic directions, which in turn initiates the formation of nanowires. For the film grown from the sample annealed at 1,100 °C, nanoparticles and nanowires/fibers ensconcing a granular morphology were seen. The SEM micrograph of this film reveals this unique fibrous and particulate morphology for TiO$_2$ (Fig. 7a, b). Figure 7a shows overlapping regions of nanograins and wires and Fig. 7b shows a few aggregated nanowires (region marked as A) that appear to originate from a porous nano-grained structure (region marked as B). A set of intermingled nanowires, abutting each other, are further elucidated as inset in Fig. 7b. The TEM image of this film (Fig. 8a) shows short length porous nanowires as the principal component in the sample annealed at 1,100 °C. The inset of Fig. 8a shows two parallel single
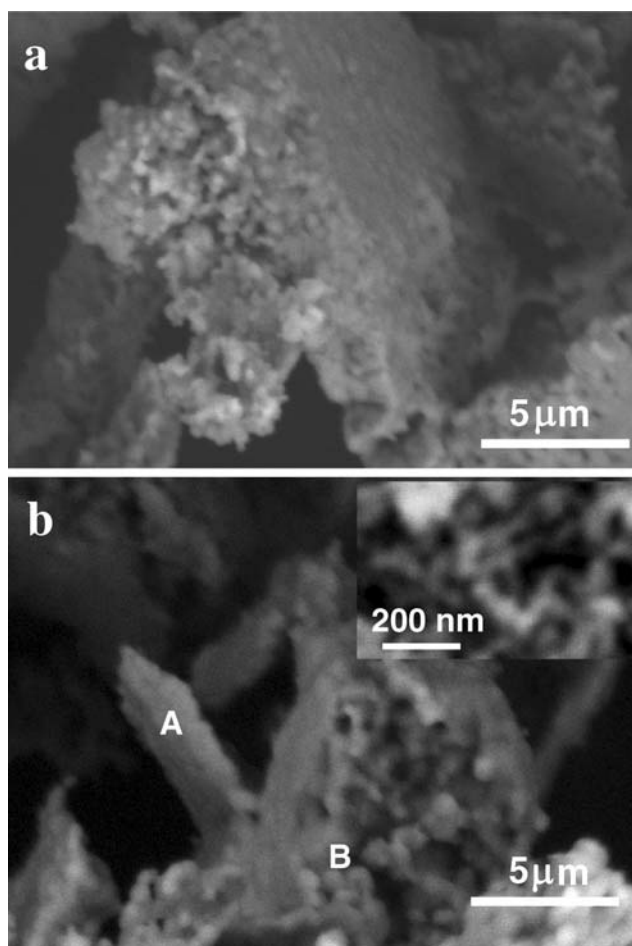

Fig. 8 TEM bright field micrographs of different annealing conditions; **a** 1,100 °C—nanowires and fibrous grains and (**b**) 1200 °C—dendritic growth. Insets are SADPs from **a** rutile along [1$\bar{1}$0] and **b** anatase along [001 zone axes

crystalline nanowires of same diameter (~10 nm) and length (~500 nm). A SADP recorded on this nanowire along the [1$\bar{1}$0] zone axis of rutile–tetragonal has been displayed as inset in Fig. 8a. However, further annealing at 1,200 °C causes the collapse of the nanowires to yield a dendrite like shape of a main stem consisted with fine branches of nanoparticles (Fig. 8b). At this stage, it was observed that the main stem (primary branch) of the dendrite continues to have a rutile structure, whereas the grains associated with secondary branches have an anatase structure. The inset of Fig. 8b shows the SADP recorded from one of these secondary branches, along the [001] zone axis of anatase crystal structure with 110 and 1$\bar{1}$0 planes marked therein.

The overall microstructural transformation can be summarized as follows: from faceted granular (up to 700 °C, Figs. 1–4) structure to fibrous grains/wires (at 1100 °C, Fig. 8a) and finally to dendrites (at 1,200 °C, Fig. 8b). The schematic in Fig. 9 shows the transformation from nano-grained microstructure below 700 °C (Fig. 9a),

Fig. 7 SEM micrographs (**a**, **b**) of samples annealed at 1,100 °C showing coexistent morphologies of fibrous (wires) and fine grains. Inset in Fig. 7b shows intermingled wires
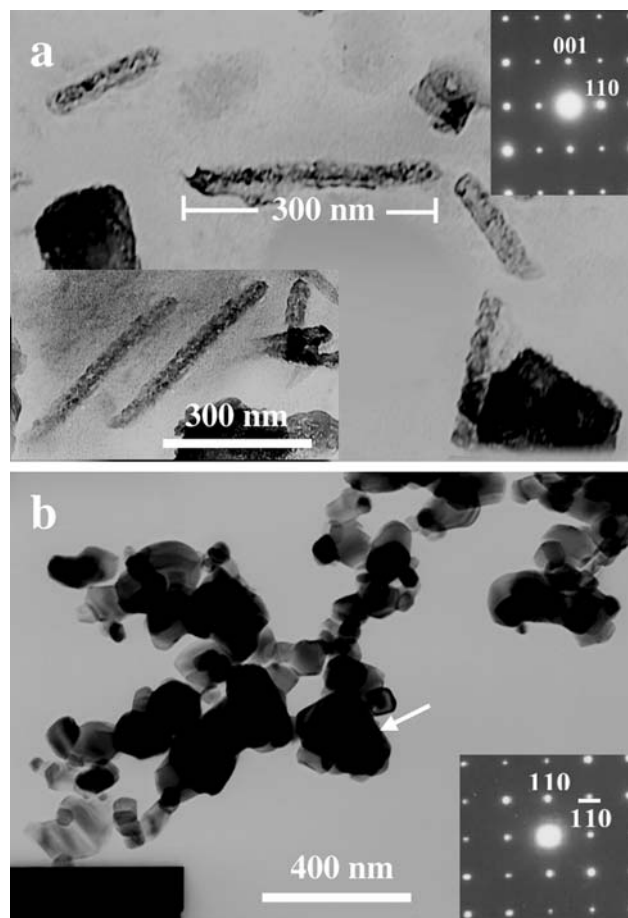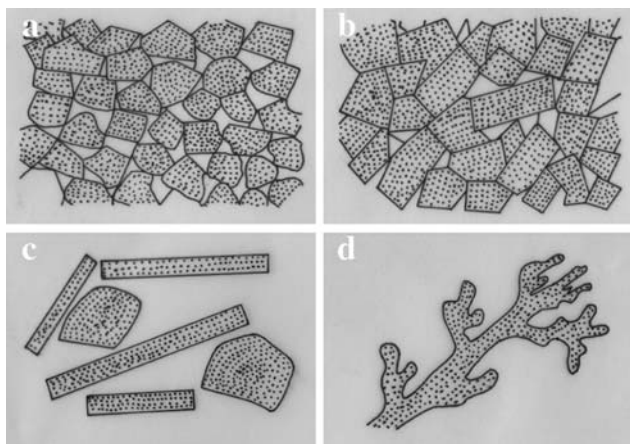
Fig. 9 Mechanism showing different microstructural transformations on annealing at temperatures: **a** as deposited, **b** 700 °C, **c** 1,100 °C, and **d** 1,200 °C

initiation of nanowire formation at 700 °C (Fig. 9b), growth of nanowires at 1,100 °C (Fig. 9c), and collapse of nanowires to ensue in dendrite like shapes at 1,200 °C (Fig. 9d). It appears that the fibrous features (at 700 °C) evolve due to solid-state phase transition, which is accompanied by lessening of strain and reduction of defects prevalent at the lattice scale in the material. The mottled contrast in the micrograph of the film annealed at 700 °C arises due to the strain present at lattice scale. Annealing allows the formation of a more thermodynamically stable microstructure and therefore wire like shapes with effective surface are higher than that of regular particles are formed at 1,100 °C. It is evident that the rutile phase triggers the growth of nanowire as at 1,200 °C when the anatase phase re-appears, the wire morphology gives way to a fibrous structure encompassing a regular granular phase.

XRD patterns of TiO_2 films annealed at different temperatures are shown in Fig. 10. For the as-deposited film,
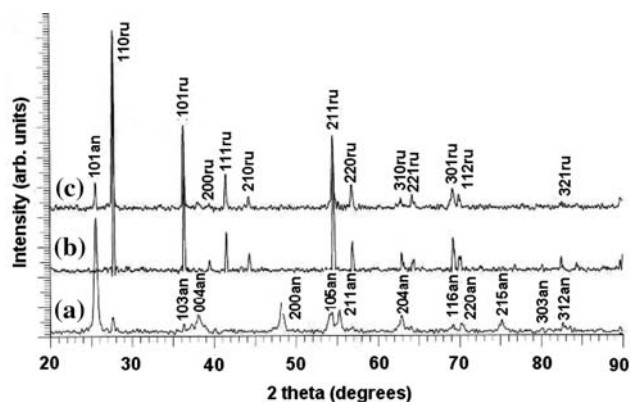
the intense peaks due to the planes (*hkl*): 101, 103, 004, 200, 105, 211, 204, 116, 220, 215, 303, 312 of the anatase phase of TiO_2 in accordance with PDF number 21-1272 corresponding to the interplanar spacings (*d*): 0.35, 0.242, 0.237, 0.187, 0.169, 0.166, 0.148, 0.136, 0.134, 0.126, 0.12, 0.117 nm, respectively, are marked on the diffractogram (Fig. 10a). At 1,100 °C, the phase transformation from anatase to rutile structure is complete as peaks corresponding to single phase rutile crystal structure with the planes (*hkl*): 110, 101, 200, 111, 210, 211, 220, 310, 221, 301, 112, 321, corresponding to interplanar spacings (*d*): 0.323, 0.247, 0.229, 0.218, 0.205, 0.166, 0.162, 0.148, 0.145, 0.136, 0.134, 0.117 nm, are seen in the diffractogram (Fig. 10b) as per PDF number 21-1276 from the JCPDS library of spectra. The partial transformation of rutile phase into anatase (as seen from TEM in Fig. 8b) on annealing the sample at 1,200 °C is also supplemented by the XRD data, as an extra peak at interplanar spacing of 0.35 nm corresponding to *hkl*:101 of anatase phase is seen in the diffractogram of this sample (Fig. 10c). All other peaks in the XRD pattern at this temperature (1,200 °C) still belong to the rutile phase.

Photoluminescence and Spectroscopy Measurements

Photoluminescence (PL) spectra recorded at room temperature from the different annealed samples (at 700, 1,100 and 1,200 °C) are depicted in Fig. 11. The emission of the samples was recorded at excitation wavelength of 200 nm, under similar excitation conditions. In all three samples, three peaks corresponding to UV, blue, and green are observed. The different emissions observed in present work can be seen from Fig. 12. E_{UV}, E_b, and E_g are energies corresponding to the emission bands maxima for the UV (414–422 nm), blue (470–483 nm), and green
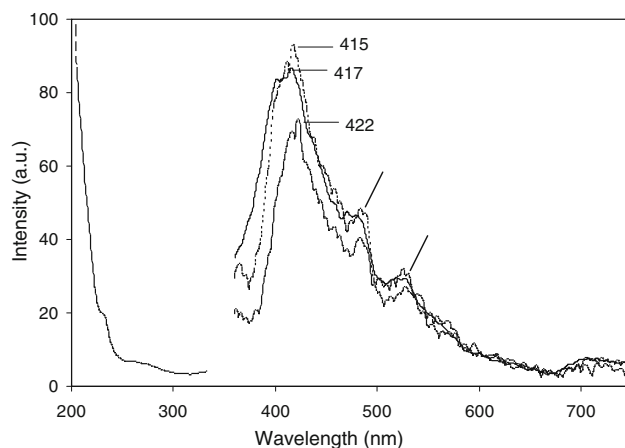

Fig. 10 XRD patterns from TiO_2 in different conditions; **a** as deposited, **b** and **c** annealed at 1,100 and 1,200 °C, respectively. an: anatase, ru: rutile

Fig. 11 Photoluminescence spectra of TiO_2 in different annealed conditions: 700, 1100, and 1,200 °C. Symbols: excitation at 205 nm (- - -); 700 °C (—); 1100 °C (…); 1200 °C (– · –)
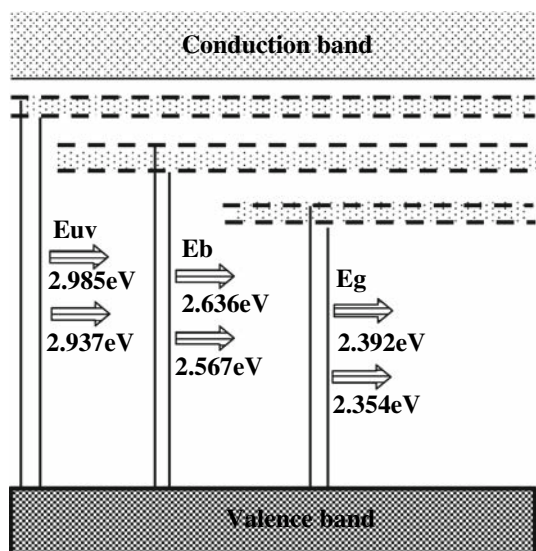
Fig. 12 Schematic showing a general energy band diagram describing the photoluminescence of nanostructured TiO_2

(518–526 nm), respectively. The UV emission originates from interband transition of electrons and the visible emission is due to transition of electrons from shallow donor level of the oxygen vacancies in the valence band. The oxygen vacancies evolved during growth of the material, trap electrons and thus become paramagnetic and give the characteristic electron spin resonance signal. When the material gets exposed to ultraviolet, these vacancies then become susceptible to trap holes generated by the UV exposure. The recombination of hole with the electron already trapped at the oxygen vacancies emits light, which is generally in the visible region. A net energy-peak shifts in all these samples, showed that the blue shift is significant ($\Delta E = 0.072$ eV, Table 1) with the annealing temperature. However, we did not observe considerable change in intensity of various bands with annealing at these temperatures (700, 1100, and 1,200 °C). In our previous study [16], the emission bands recorded up to maximum annealing temperature of 700 °C showed a trend of decreasing PL intensity with increasing temperature and the observations were understood on the basis of the various processes such as self-trapped excitons recombination which is a combined effect of defect centres generated from oxygen vacancies and particle size variation. In the

present case, a dominant blue shift with increasing annealing temperature with considerable variation in PL intensity may be attributed to structural transformation from anatase to rutile and then partial transformation of rutile to anatase on increasing annealing temperature.

Raman spectra of TiO_2 films are shown in Fig. 13. Raman bands in anatase phase (in as-deposited condition) exist at Raman shifts corresponding to 398 ($B1_g$), 515 ($A1_g$) and 640 (E_g) cm^{-1} of vibrational modes. In contrast, the Raman bands in rutile phase (annealing at 1,100 °C) reveals frequencies at 448 (E_g) and 612 ($A1_g$) cm^{-1} of corresponding vibrational modes. However, the prior studies have further been confirmed by studying the samples annealed at 1,200 °C. A weak Raman shift (515 cm^{-1}, $A1_g$ of anatase phase) in addition to strong peaks (448, 612 cm^{-1}:E_g and $A1_g$ of rutile phase) shows that there is a partial phase transition of rutile to anatase at 1,200 °C. The peak shifts arise due to different influences on change in the polarizability of electronic structures of rutile and anatase (although both are tetragonal with the same group: D^{19}_{4h}).
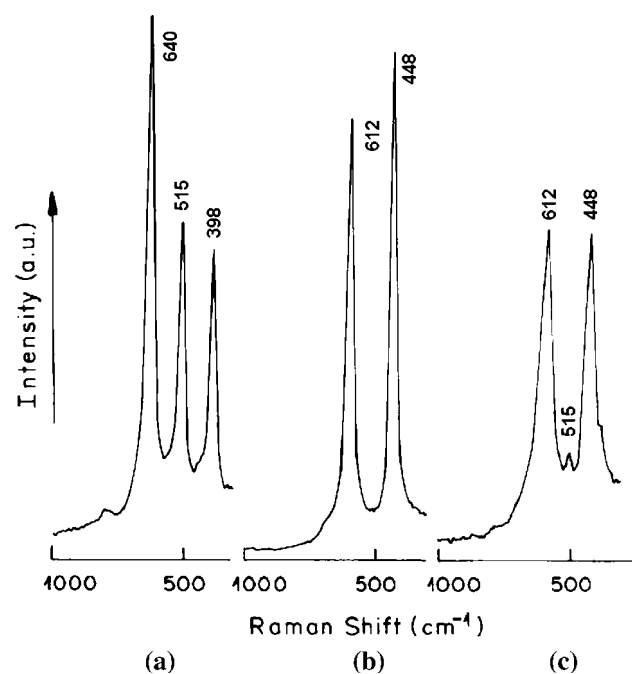

Fig. 13 Raman spectra of TiO_2 in different conditions; **a** as deposited, **b** and **c** annealed at 1,100 and 1,200 °C, respectively

Table 1 Effect of annealing conditions on different photoluminescent emission peaks of TiO_2

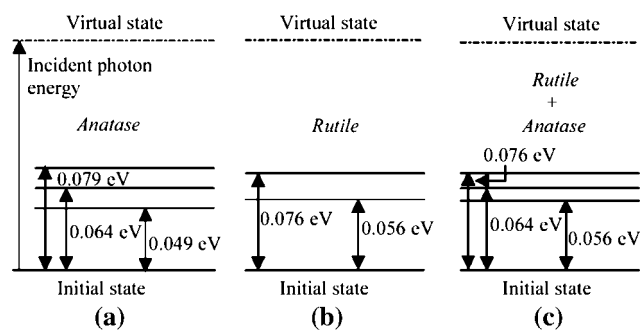| Annealing conditions	700 °C		1100 °C		1200 °C		Peak shift in PL emission	
PL peak	λ (nm)	E (eV)	λ (nm)	E (eV)	λ (nm)	E (eV)	$\Delta\lambda$ (nm)	ΔE (eV)
UV	414.43	2.985	417.00	2.974	422.24	2.937	7.81	0.048
Blue	470.50	2.636	483.65	2.564	483.13	2.567	2.63	0.072
Green	518.48	2.392	525.01	2.362	526.94	2.354	7.46	0.038

Fig. 14 Vibrational energy level diagrams for Raman scattering from TiO_2 in different conditions; **a** as deposited, **b** and **c** annealed at 1,100 and 1,200 °C, respectively

The corresponding energy level diagram for Raman scattering (Fig. 14) in the present work shows the peak due to anatase at high temperatures (1,200 °C) although this phase is not a thermodynamically stable phase and is not revealed between 700 and 1,100 °C. The optical phonon energies corresponding to different vibrational modes in anatase and rutile phases are very small, but the fine structural changes at lattice scale are significantly visible in the energy band diagram. The fine energy shifts in UV, blue, and green emissions in photoluminescence are also dependent on these vibrational states upon photoexcitation. For example the energy-shifts in photoluminescence at different annealing conditions in UV, blue, and green as plotted in Fig. 4, 0.048, 0.072, and 0.038 eV, respectively, (Table 1) are of the order of Raman active vibrations (Fig. 14) in different anatase and rutile structures of TiO_2. This implies that the Raman active optical phonons are excited due to external energy and subsequently assist the band-to-band recombination (UV region) and transitions due to different surface states and defects (blue and green region). It has been stated [19] that the band-to-band recombination (anatase phase) can be considered as a two phonons $(E_g(v_5):0.017 \text{ eV} + E_g(v_6):0.024 \text{ eV} = 0.041 \text{ eV})$—one photon (0.04 eV) coupling course. The kinetics of the conversion of anatase to rutile has been studied in the past [17] by Raman spectroscopy. Authors in [17] observed a sequential change in intensity of the anatase form were observed with laser irradiation time and it was noticed that there is a rise of 236 cm^{-1} (rutile) and fall of 515 cm^{-1} (anatase). But in the present work at high temperature (1,200 °C) the initiation of 515 cm^{-1} (anatase) and a sharp decrease in intensity of 44 and 612 cm^{-1} (rutile) bands has been observed for the first time. This is possible only if the TiO_6 octahedra (rutile at 1,100 °C) is distorted at 1,200 °C in such a way that it tends to achieve anatase-crystallographic symmetry and in this process a vibrational mode of anatase at 515 cm^{-1} is seen in the Raman spectrum. Since the transformation of rutile to anatase is not complete at this

temperature (1,200 °C), bands at 448 and 612 cm^{-1} of rutile phase continue to exist in the spectrum.

Conclusions

Nano-scaled morphological and crystallographic transformations in a sol–gel derived TiO_2 have been studied employing highly precise and complementary techniques like TEM, XRD, and Raman spectroscopy. The nanostructural transformations from particles to wires initiate at 700 °C and significant growth of wires takes place at 1,100 °C. However, our further investigations have delineated that at 1,200 °C the wires undergo a nanostructural instability and leads to branching on nanowires. Nanoscaled features obtained on annealing at different temperatures are related with the different crystal structures of TiO_2. Wire formation takes place when the anatase phase transforms to rutile structure of TiO_2 (annealed at 700–1100 °C). A noteworthy feature was delineated as the rutile phase partially transforms to anatase again at 1,200 °C. Moreover these different nano-objects have been further evaluated for their performance as luminescent materials.

References

1. H. Gleiter, Acta Mater. **48**, 1 (2000). doi:10.1016/S1359-6454(99)00285-2
2. H.S. Nalwa, *Handbook of Nanostructured Materials and Nanotechnology* (Academic Press Publishing, Tokyo, 2000)
3. F. Carlier, S. Benrezzak, P. Cahuzac, N. Kébaïli, A. Masson, A.K. Srivastava, C. Colliex, C. Bréchignac, Nano. Lett. **6**, 1875 (2006). doi:10.1021/nl060781n
4. Z.L. Wang, J. Phys.: Condens. Matter. **R829**, 16 (2004)
5. M.H. Huang, S. Mao, H. Feick, H. Yan, Y. Wu, H. Kind, E. Weber, R. Russo, P. Yang, Science **292**, 1897 (2001). doi:10.1126/science.1060367
6. A.K. Srivastava, K.N. Sood, K. Lal, R. Kishore, Patent Filed Ref. No. 0773DEL2005, 31 March 2005
7. A.K. Srivastava, N. Gupta, K. Lal, K.N. Sood, R. Kishore, J. Nanosci. Nanotech. **7**, 1941 (2007)
8. H. Bahadur, A.K. Srivastava, R.K. Sharma, S. Chandra, Nanoscale Res. Lett. **2**, 469 (2007). doi:10.1007/s11671-007-9089-x
9. A.K. Srivastava, S.A. Agnihotry, M. Deepa, Thin Solid Films **515**, 1419 (2006). doi:10.1016/j.tsf.2006.03.055
10. M. Deepa, A.K. Srivastava, S.A. Agnihotry, Acta Mater. **55**, 6095 (2006). doi:10.1016/j.actamat.2007.07.056
11. M. Deepa, A.K. Srivastava, S.A. Agnihotry, J. Phys. D: Appl. Phys. **39**, 1885 (2006)
12. M. Deepa, A.K. Srivastava, K.N. Sood, S.A. Agnihotry, Nanotechnology **17**, 2625 (2006). doi:10.1088/0957-4484/17/10/030

13. J.M. Wu, H.C. Shih, W.T. Wu, Nanotechnology **17**, 105 (2006). doi:10.1088/0957-4484/17/1/017
14. Z. Miao, D. Xu, J. Ouyang, G. Guo, X. Zhao, Y. Tang, Nano. Lett. **2**, 717 (2002). doi:10.1021/nl025541w
15. G.K. Mor, K. Shankar, M. Paulose, O.K. Varghese, C.A. Grimes, Nano. Lett. **6**, 215 (2006). doi:10.1021/nl052099j
16. S. Bhandari, M. Deepa, A.K. Srivastava, S.T. Lakshmikumar, Ramakant, Solid State Ion (2008). doi:10.1016/j.ssi.2008.10.008
17. S.J. Rigby, A.H.R.A. Obaidi, S.K. Lee, D. McStay, P.K.J. Robertson, Appl. Surf. Sci. **252**, 7948 (2006). doi:10.1016/j.apsusc.2005.10.003
18. C.A. Melendres, A. Narayansamy, V.A. Maroni, R.W. Siegel, J. Mater. Res. **4**, 1248 (1989). doi:10.1557/JMR.1989.1246
19. B. Liu, L. Wen, X. Zhao, Mater. Chem. Phys. **106**, 350 (2007). doi:10.1016/j.matchemphys.2007.06.012
20. B. Liu, L. Wen, X. Zhao, Sol. Energy Mater. Sol. Cells **92**, 1 (2008). doi:10.1016/j.solmat.2007.07.009
21. A.K.Srivastava, M. Deepa, H.-J. Kleebe, H. Fuess, S. Bhandari, IEEE 978-1-4244-1727-8, 866 (2007)
22. O.K. Varghese, D. Gong, M. Paulose, K.G. Ong, C. Dickey, C.A. Grimes, Adv. Mater. **15**, 624 (2003). doi:10.1002/adma.200304586
23. E.G.J. Wijnhoven, W.L. Vos, Science **281**, 802 (1998). doi:10.1126/science.281.5378.802
24. A. Richel, N.P. Johnson, D.W. McComb, Appl. Phys. Lett. **76**, 1816 (2000). doi:10.1063/1.126175
25. G. Dagan, M. Tomkiewics, J. Phys. Chem. **97**, 12651 (1993). doi:10.1021/j100151a001
26. O. Regan, M. Grätzel, Nature **353**, 737 (1991). doi:10.1038/353737a0
27. O. Diwald, T.L. Thompson, T. Zbkov, G.E. Goralski, S. Walck, J.J. Yates, J. Phys. Chem. B **108**, 6004 (2004). doi:10.1021/jp031267y
28. J. Sun, L. Gao, Q. Zhang, J. Am. Ceram. Soc. **86**, 1677 (2003)
29. Q. Ming, Z.Y. Zhen, Y.J. Hong, Z. Jun, Mater. Sci. Eng. A **434**, 71 (2006). doi:10.1016/j.msea.2006.07.043
30. D.K. Dwivedi, Mater. Sci. Eng. A **382**, 328 (2004). doi:10.1016/j.msea.2004.05.014
31. C. Eriksson, J. Lausmaa, H. Nygren, Biomaterials **22**, 1987 (2001). doi:10.1016/S0142-9612(00)00382-3
32. S.J. Botha, Mater. Sci. Eng. A **243**, 221 (1998). doi:10.1016/S0921-5093(97)00805-8